Ground-Based Soil Moisture Retrieval Using the Correlation Between Dual-Polarization GNSS-R Interference Patterns

El Hajj, Marcel M.; Steele-Dunne, Susan C.; Almashharawi, Samer K.; Tian, Xuemeng; Johansen, Kasper; Camargo, Omar A.Lopez; Amezaga-Sarries, Adria; Mas-Vinolas, Andreu; McCabe, Matthew F.

DOI
10.1109/TGRS.2023.3337841

Publication date
2024

Document Version
Final published version

Published in
IEEE Transactions on Geoscience and Remote Sensing

Ground-Based Soil Moisture Retrieval Using the Correlation Between Dual-Polarization GNSS-R Interference Patterns

Marcel M. El Hajj, Susan C. Steele-Dunne, *Member, IEEE*, Samer K. Almashharawi, Xuemeng Tian, Kasper Johansen, Omar A. López Camargo, *Student Member, IEEE*, Adria Amezaga-Sarries, Andreu Mas-Viñolas, and Matthew F. McCabe

***Abstract*— Soil moisture (SM) is an important state variable in land surface models. Here, we investigate the potential of a ground-based global navigation satellite system receiver with two linearly polarized antennas that measure the interference power (IP) of direct and reflected signals in horizontal polarization (H-pol) and vertical polarization (V-pol) to estimate SM. The coefficient of determination between the IP waveforms at H-pol and V-pol ($R^2_{v/h}$) was used as a predictor of SM. A coherent specular reflection model was employed to first explore the relationship between $R^2_{v/h}$ and SM for different values of soil roughness. That relationship was subsequently applied to estimate SM from $R^2_{v/h}$ determined from global positioning system (GPS) signals acquired continuously by a ground-based receiver between May and December 2022 for an area with very smooth bare soil. The results show that the proposed method can estimate the SM of the upper 10-cm layer with high accuracy (with a root-mean-square error (RMSE) of approximately 1.5 vol.%) and demonstrate the potential of the ground-based IP technique as a practical system solution for proximal remote sensing of SM over bare soils.**

***Index Terms*— Global navigation satellite systems reflectometry (GNSS-R), interference power (IP), soil moisture (SM).**

I. Introduction

SOIL moisture (SM) is a key variable routinely used to understand and predict the behavior of Earth's climate and water cycle. Active and passive X-, C-, and L-band microwave sensors are the primary remote sensing systems used to estimate SM over large spatial extents. Synthetic aperture radar (SAR) satellites, such as Sentinel-1 (C-band), have shown great potential for repetitive mapping over both large areas and at small plot scales [1], [2], [3]. However, SAR C-band backscattering is not sensitive to the SM underneath well-developed crop canopy cover and often provides overestimation or underestimation in the case of rough and smooth soils, respectively [1], [4]. While passive radiometry satellites map SM with a higher revisit time than SAR systems, they provide much lower spatial resolution (between 10 and 50 km). Importantly, the brightness temperature measured by satellites can be significantly disturbed by interferences from anthropogenic radio wave sources from the ground [5], [6], [7].

Over the past decade, global navigation satellite systems reflectometry (GNSS-R) techniques, which measure the direct signal from global positioning system (GPS) satellites as well as the reflected signal from the Earth's surface, have emerged as a "signal of opportunity" [8] for continuous and near real-time SM estimation. Since 2007, multipath signals have been used to estimate SM, primarily through three ground-based GPS receiver setup configurations [9], [10], [11], [12], [13]. The first configuration uses two antennas, one looking toward the zenith to acquire the direct signal at the right-hand circular polarization and the other looking toward the ground (nadir) to acquire the reflected (multipath) signal at the left-hand circular polarization. With this ground-based GPS receiver configuration, SM can be estimated from the reflection coefficient computed by dividing the averaged waveforms from direct and reflected GNSS signals [13]. The second configuration employs an interferometric GNSS-R ground-based receiver with a single antenna, and it estimates SM by analyzing the phase, amplitude, and frequency of the interference pattern between the direct and reflected signals [9], [10], [11]. The third ground-based receiver configuration is known as the interference pattern technique (IPT). It employs a dual-polarized antenna oriented horizontally to measure the power fluctuations of the interference of direct and reflected signals at horizontal polarization (H-pol) and vertical polarization (V-pol).

With the IPT technique, SM is currently estimated by determining the so-called notch position θ_B: the angular elevation value (i.e., θ) of the smallest interference power (IP) oscillation at V-pol [12]. SM is estimated from θ_B following a quasi-linear law, where θ_B decreases between $\sim$27° and $\sim$15° as SM increases between 5 vol.% and 40 vol.% [12], [14]. To determine θ_B, Rodriguez-Alvarez et al. [12] computed

Manuscript received 10 August 2023; revised 2 November 2023; accepted 23 November 2023. Date of publication 30 November 2023; date of current version 19 December 2023. This work was supported by the King Abdullah University of Science and Technology. *(Corresponding author: Marcel M. El Hajj.)*

Marcel M. El Hajj, Samer K. Almashharawi, Kasper Johansen, Omar A. López Camargo, and Matthew F. McCabe are with the Hydrology, Agriculture and Land Observation (HALO) Laboratory, Division of Biological and Environmental Sciences and Engineering, King Abdullah University of Science and Technology (KAUST), Thuwal 23955-6900, Saudi Arabia (e-mail: marcel.elhajj@kaust.edu.sa).

Susan C. Steele-Dunne is with the Department of Geoscience and Remote Sensing, Delft University of Technology, 2628 CN Delft, The Netherlands.

Xuemeng Tian was with the Department of Geoscience and Remote Sensing, Delft University of Technology, 2628 CN Delft, The Netherlands. She is currently with the Laboratory of Geo-information Science and Remote Sensing, Wageningen University and Research, 6708 PB Wageningen, The Netherlands, and also with OpenGeoHub Foundation, 6708 PW Wageningen, The Netherlands.

Adria Amezaga-Sarries and Andreu Mas-Viñolas are with Microwave Sensors and Electronics SL, 08720 Barcelona, Spain.

Digital Object Identifier 10.1109/TGRS.2023.3337841

(a) (b) (c)

Fig. 1. (a) From the top of the pole to the bottom, the SMIGOL-R instrument installed at 4.75 m, the power supply system for the SMIGOL-R, the solar panel to charge the power supply of the SMIGOL, the solar panel, and the data logger for the SM sensors. (b) Close image of the soil showing the very smooth surface (roughness ∼0.5 cm). (c) Another view angle of the installed system showing the irrigated area.

the upper and lower envelopes of the IP waveform (i.e., IP variation as a function of θ) at V-pol. θ_B is then θ where the difference between the upper and lower envelopes is the smallest. Arroyo et al. [14] estimated θ_B by computing the phase difference between IP at H-pol (IP-H) and IP at V-pol (IP-V). They first retrieved the positions of maxima and minima points in IP-H and IP-V waveforms. Then, for each polarization, the first relative maximum or minimum is taken as a reference, and from there, the entire phase of the interference pattern for that polarization is inferred, given that the phase difference between consecutive relative maxima or minima is 180°. θ_B is equal to θ when a phase difference between IP-H and IP-V equal to 90° is observed. Alvarez et al. [12] and Arroyo et al. [14] found it challenging to accurately determine θ_B in real GNSS-R acquisitions, especially when the IP waveform exhibits low-frequency oscillations or maintains constant amplitude over a wide range of θ. This complexity is particularly evident in operational GNSS-R applications. Inaccurate estimation of θ_B leads to inaccurate estimation of SM, as θ_B is highly sensitive to moisture variations. Indeed, a variation of 1° of θ_B corresponds approximately to a variation of 2.5 vol.% in SM [12]. Therefore, a more robust and practical method to estimate SM from IP-H and IP-V waveforms is needed.

This work advances the study of [14] by developing a more practical and robust method to estimate SM over bare soil using both IP-H and IP-V waveforms. In this study, IP-H and IP-V were recorded by a ground-based GPS receiver, the SM interference-pattern GNSS observations at L-band reflectometer (SMIGOL-R), installed on a patch of bare soil in Saudi Arabia. The estimation of SM from SMIGOL-R was validated using continuous in situ SM measurements collected between May and December 2022.

II. SMIGOL-R Instrument and Experimental Details

The ground-based GPS receiver, SMIGOL-R, has a dual-polarized antenna and was developed by Microwave Sensors and Electronics (https://www.mwse.tech/). The SMIGOL-R was used to measure the instantaneous IP (IP-H and IP-V) from the direct and reflected GPS L1-band signals (1.57542 GHz). The SMIGOL-R was placed at a height of 4.75 m above the ground on a patch of bare soil at a study site in the Al-Jawf region of Saudi Arabia (38.322986°, 29.858745°) with the antenna oriented horizontally at an azimuth angle of approximately 175° (Fig. 1).

The SMIGOL measures the variation of the IP as the GPS satellites move, so the measured IP is a function of the satellite θ. The reflected signal on the Earth's surface that is recorded by the system is that scattered from the so-called Fresnel zone, which is the area around the specular point from where the scattered signals are collected, with a normalized scattering coefficient that is higher than $1/e$ [12]. The Fresnel zone has an elliptical shape facing the antenna, and its dimensions depend on antenna height, soil roughness, and satellite elevation angle. For an antenna height of 4.75 m, a maximum extension for the Fresnel zone of approximately 40 × 1 m is feasible [12].

The SMIGOL antenna is a symmetrical probe-feed patch antenna featuring two probes for each polarization. Each set of probes for a specific polarization is connected to a 180° hybrid circuit (resulting in two 180° hybrids). This arrangement is carefully designed to achieve a symmetric antenna and ensure a radiation pattern that is uniform in all directions. The ultimate goal is to maintain a consistent gain for a given elevation angle and its corresponding negative

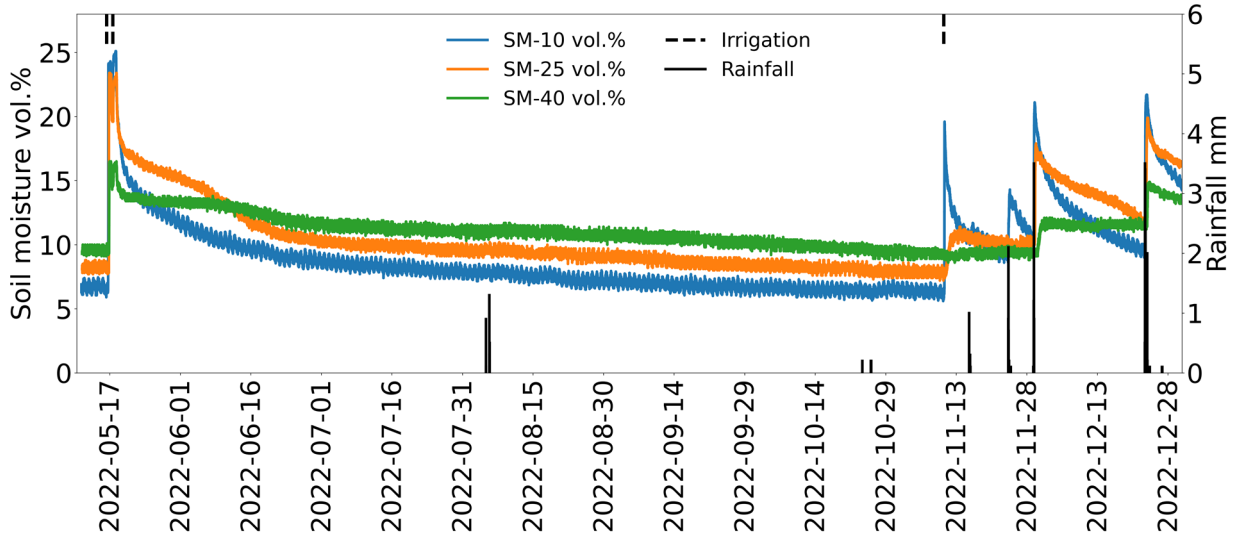

Fig. 2. Temporal variations of SM at 10 (SM-10), 25 (SM-25), and 40 (SM-40) cm depths. Vertical lines show rainfall events. Vertical dashed lines show irrigation activities.

elevation angle, thus preventing any introduction of aberrations into the interference pattern. The patch antenna is fabricated using a Rogers RO4003 substrate and boasts a beamwidth of ±40°, along with a gain typical of a patch antenna, measuring approximately 6 dB. To safeguard the antenna, it is enclosed within a protective Teflon radome.

For the investigation period (May–December 2022), the average daily air temperature ranged from 30 °C in May, 40 °C in August, and 15 °C in December. The maximum air temperatures of up to 47 °C were recorded in August. Rain events were rare and occurred mostly between November and December, with a cumulative rainfall of 29 mm over the study period. As rainfall is scarce, two irrigation experiments were conducted on May 16 and 17 and November 10, 2022, using five sprinklers to induce spatial variability in the SM conditions. The irrigated area was located in front of the antenna and extended over an elliptical area with dimensions of 50 × 20 m, thus encompassing the size of the Fresnel zone. In the first irrigation experiment, irrigation was triggered on May 16, 2022 at 17:00 and on May 17, 2022 at 18:00, for a duration of 8 h each. In the second irrigation experiment, irrigation was triggered once on November 10, 2022 at 10:00 for a duration of 3 h. In situ SM was recorded by ThetaProbe sensors every 15 min at 10 cm (SM-10) (two sensors with the average moisture value considered), 25 cm (SM-25), and 40 cm (SM-40) depths (Fig. 2).

Prior to the first irrigation activity, on May 12, 2022, SM-10, SM-25, and SM-40 values were approximately 7.5, 8.5, and 9.5 vol.%, respectively (Fig. 2). During the first irrigation activity, the values of SM-10 and SM-25 reached the maximum values of 25.0 vol.%, while the values of SM-40 reached a lower value of 16.5 vol.%. This indicates that the amount of infiltrated water is reduced beyond a depth of >25 cm. After the first irrigation, SM-10 dried out faster than SM-25, and the latter, in turn, dried out faster than SM-40, due to higher evaporation rates in the upper soil layers. In the absence of irrigation and rainfall, SM-10, SM-25, and SM-40 continued to decrease. A similar behavior of SM was observed in the second irrigation activity performed on November 10, 2022, and after rain events occurring after November 13, 2022 (Fig. 2).

III. Method

In this study, the SM was estimated from the coefficient of determination, $\boldsymbol{R}^2_{v/h}(1)$, between the IP-H and IP-V waveforms. Arroyo et al. [14] observed that for θ between 5° and 30°, the IP-H and IP-V waveforms are in-phase for $\theta < \theta_B$, while they are in counter phase for $\theta > \theta_B$. Accordingly, in extremely dry conditions when θ_B is ∼27° [12], almost the whole IP-H and IP-V waveforms are oscillating in-phase, thus yielding a high $\boldsymbol{R}^2_{v/h}$ value. Inversely, in extremely wet conditions, when θ_B is around 5° [12], almost the entire IP-H and IP-V waveforms are oscillating in counter phase, thus yielding a low $\boldsymbol{R}^2_{v/h}$ value. However, the relationship between $\boldsymbol{R}^2_{v/h}$ and SM variations remains unknown. To address this knowledge gap, we used simulations from the coherent specular reflection model [15]

$$\boldsymbol{R}^2_{v/h} = \left(\frac{\sum (x - mx)(y - my)}{\sqrt{\sum (x - mx)^2 \sum (y - my)^2}} \right)^2 \quad (1)$$

where x and y represent the amplitude of the IP-H and IP-V waveforms at each GPS elevation angle, respectively, and mx and my denote the respective averages of the IP-H and IP-V waveforms.

A. Coherent Specular Reflection Model

The coherent specular reflection model [15] was implemented to explore the relationship between $\boldsymbol{R}^2_{v/h}$ and SM, as this relation has not previously been examined in detail. Here, only a brief description of the model is presented as the model equations, and derivation and further details are explained in [12]. The simulated IP waveform at a given polarization is a coherent addition of the signal received from the

GPS satellite (direct signal) and the reflected signal (multipath) altered by the soil parameters, both received simultaneously by the SMIGOL-R. In the coherent specular reflection model, the Fresnel reflection coefficients are used to simulate the reflected signal, as we assume that the reflection surface of the study area was smooth enough to accomplish the Rayleigh criterion of smooth soil (i.e., the soil surface is smooth with respect to the GPS wavelength) [16]. The Fresnel reflection coefficients for H-pol and V-pol for a single interface between two soil layers (i and $i+1$) are computed as follows:

$$r_{h_{i,i+1}} = \frac{\sqrt{\varepsilon_{r_i} - \varepsilon_{r_i}\sin^2\theta_{\text{inc}}} - \sqrt{\varepsilon_{r_{i+1}} - \varepsilon_{r_i}\sin^2\theta_{\text{inc}}}}{\sqrt{\varepsilon_{r_i} - \varepsilon_{r_i}\sin^2\theta_{\text{inc}}} + \sqrt{\varepsilon_{r_{i+1}} - \varepsilon_{r_i}\sin^2\theta_{\text{inc}}}} \tag{2}$$

$$r_{v_{i,i+1}} = \frac{\varepsilon_{r_{i+1}}\sqrt{\varepsilon_{r_i} - \varepsilon_{r_i}\sin^2\theta_{\text{inc}}} - \varepsilon_{r_i}\sqrt{\varepsilon_{r_{i+1}} - \varepsilon_{r_i}\sin^2\theta_{\text{inc}}}}{\varepsilon_{r_{i+1}}\sqrt{\varepsilon_{r_i} - \varepsilon_{r_i}\sin^2\theta_{\text{inc}}} + \varepsilon_{r_i}\sqrt{\varepsilon_{r_{i+1}} - \varepsilon_{r_i}\sin^2\theta_{\text{inc}}}} \tag{3}$$

where $r_{h_{i,i+1}}$ and $r_{v_{i,i+1}}$ are the reflection coefficients from the interface between layers (i and $i+1$) for H-Pol and V-Pol, respectively. ε_{r_i} and $\varepsilon_{r_{i+1}}$ are the dielectric constants of layers i and $i+1$, respectively. θ_{inc} is the satellite incidence angle (90–θ). The surface reflection coefficient at q polarization can be computed for n-layers as the sum of $r_{i,i+1}+r_{i+1,i+2}+r_{i+2,i+3}+\cdots+r_{n-1,n+1}$. For the sake of simplicity, a three-layer reflection model for bare soil (air and two soil layers) was used. Equation (3) shows the implementation of the three-layer model used

$$R_{q,\text{total}} = e^{-\left(\frac{4\pi\sigma}{\lambda}\right)^2}\frac{r_{i,i+1} + r_{i+1,i+2}.e^{S}.e^{j.2\varphi}}{1 + r_{i+1,i+2}.r_{i+1,i+2}.e^{S}.e^{j.2\varphi}} \tag{4}$$

where σ is the surface soil roughness, λ is the wavelength, S is the surface's roughness correction factor, and φ is the phase term associated with the interaction between layers. Finally, the total received power by the antenna from both the reflected and direct signals is simulated as follows:

$$P = F(\theta)|1 + R_{q,\text{total}}.e^{j\emptyset}| \tag{5}$$

where $F(\theta)$ is the antenna radiation pattern and $\emptyset$ is the phase difference due to different electrical paths between the direct and reflected signals. The phase difference $\emptyset$ is calculated from the antenna height (h_a), incidence angle (θ_{inc}), and wavelength (λ) with the following equation:

$$\emptyset = \frac{4\pi}{\lambda}h_a\cos\theta_{\text{inc}}. \tag{6}$$

B. SM Estimation From Correlation Between IP-H and IP-V

The coherent specular reflection model [15] was used to explore the relationship between $\boldsymbol{R^2_{v/h}}$ and SM for different surface soil roughness values ($\sigma = 0.5$, $\sigma = 1$, and $\sigma = 2$ cm). With the coherent specular reflection model, IP-H and IP-V waveforms were simulated for moisture values between 5 vol.% and 30 vol.% at intervals of 5 vol.% and for different surface soil roughness values ($\sigma = 0.5$, $\sigma = 1$, and $\sigma = 2$ cm). The simulation was done by considering an antenna height equal to the installed SMIGOL-R height (4.75 m) (6). In addition, a soil composition of 78% sand, 10% silt, and 12% clay was used in the simulations to compute the dielectric constant (ε) in (2) and (3). ε was computed from soil composition and SM using equations developed in [17]. Then, for each roughness condition, the relationship between $\boldsymbol{R^2_{v/h}}$ (computed on simulated IP-H and IP-V waveforms) and SM (between 5 vol.% and 30 vol.% with a step of 5%) was established. To estimate the SM, the relationship obtained between $\boldsymbol{R^2_{v/h}}$ and SM via simulations with the coherent specular reflection model was later applied to $\boldsymbol{R^2_{v/h}}$ calculated based on the actual IP-H and IP-V waveforms recorded by SMIGOL-R. Finally, the SMIGOL-R derived SM was compared to in situ SM-10, SM-25, and SM-40 using root-mean-square error (RMSE) and bias (estimated-reference) for evaluation.

IV. Results and Discussion

A. Relationship Between $\boldsymbol{R^2_{v/h}}$ and SM Using Simulated IP-V and IP-H

The coherent specular reflection model [15] was used to explore the relationship between $\boldsymbol{R^2_{v/h}}$ and SM (between 5 and 30 vol.%) for different levels of roughness ($\sigma = 0.5$, $\sigma = 1$, and $\sigma = 2$ cm). The simulation presented in Fig. 3 shows that θ_B depends on SM variation (θ_B decreases as SM increases) but does not depend on σ variation [12]. For instance, for all σ values (0.5, 1, and 2 cm), θ_B was equal to 24.88°, 18.71°, and 13.86° for SM of 10 vol.%, 20 vol.%, and 30 vol.%, respectively (Fig. 3). Furthermore, the simulation showed that the IP-H and IP-V waveforms are in-phase and in counter phase when $\theta < \theta_B$ and $\theta > \theta_B$, respectively. As an example, for SM = 30 vol.% and $\sigma = 1$ cm [Fig. 3(g)], IP-H and IP-V waveforms oscillate in-phase when $\theta < \theta_B$ ($\theta_B = 13.86°$). However, for $\theta > \theta_B$ ($\theta_B = 13.86°$), IP-H and IP-V waveforms begin to oscillate in counter phase, and the difference in phase level increases as θ increases. These results are in accordance with those obtained in the study in [14].

Importantly, the simulation results confirm the potential use of $\boldsymbol{R^2_{v/h}}$ to estimate SM. Indeed, θ_B changes the position with SM variation, which changes the portion of the IP-H and IP-V waveforms that are in-phase and in counter phase. This also results in $\boldsymbol{R^2_{v/h}}$ changing with SM, with low $\boldsymbol{R^2_{v/h}}$ for high values and high $\boldsymbol{R^2_{v/h}}$ for low values of SM. Considering an SM = 10 vol.% ($\theta_B = 24.88°$), the portion where IP-H and IP-V waveforms oscillate in-phase is larger than when SM = 30 vol.% ($\theta_B = 13.86°$), meaning that $\boldsymbol{R^2_{v/h}}$ at 10 vol.% SM will be higher than when at 30 vol.% SM (Fig. 3). Fig. 4 shows the relationship between $\boldsymbol{R^2_{v/h}}$ and moisture for different levels of σ. $\boldsymbol{R^2_{v/h}}$ is highly correlated with SM and the obtained relationship does not depend on σ. The absence of any effects of σ on the relation between $\boldsymbol{R^2_{v/h}}$ and moisture was expected because θ_B was found not to be dependent on σ (Fig. 3) [12].

B. Sensitivity of $\boldsymbol{R^2_{v/h}}$ to SM Variation

We evaluated the sensitivity of $\boldsymbol{R^2_{v/h}}$ values computed on actual IP-H and IP-V waveforms measured by the SMIGOL-R instrument in response to changes in SM. To illustrate the sensitivity of $\boldsymbol{R^2_{v/h}}$, four representative IP waveforms acquired

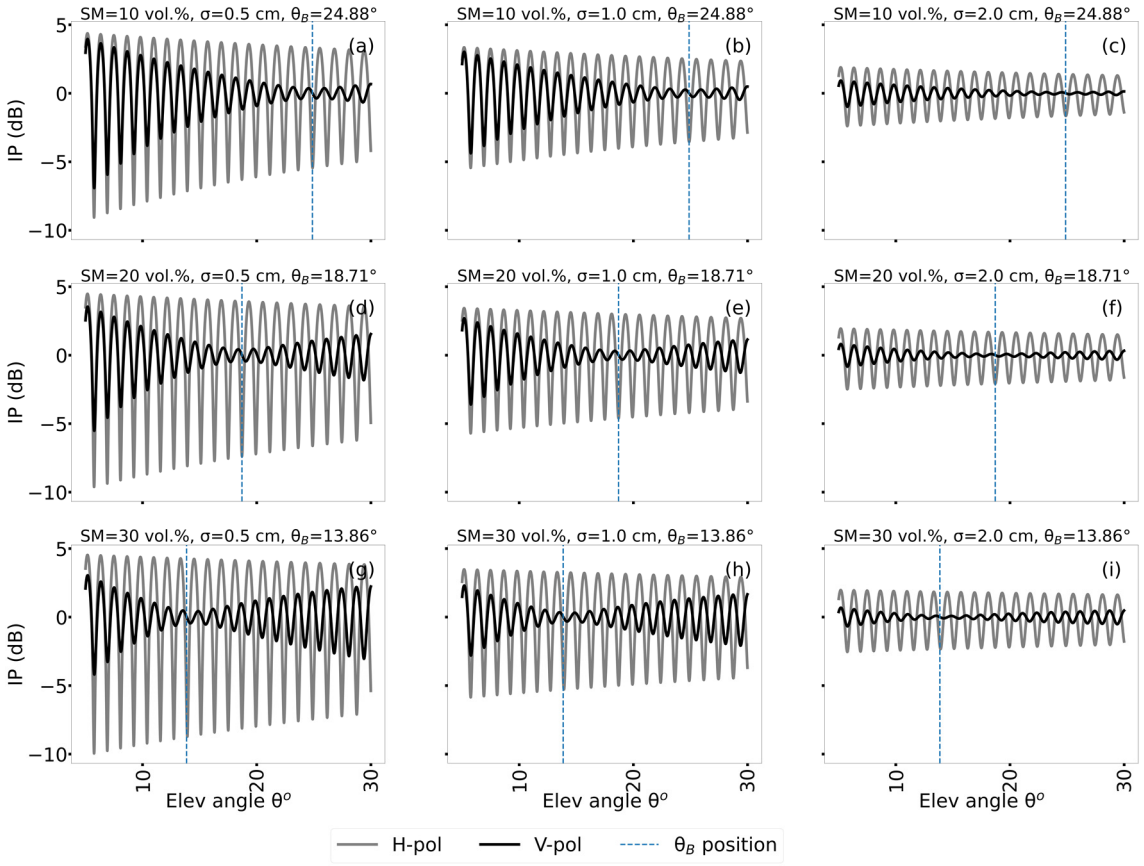

Fig. 3. Simulation of IP in decibels (dB) for satellite elevation angles between 5° and 30° (a)–(i). The simulation was performed for SMs of 10 vol.%, 20 vol.%, and 30 vol.% and for three levels of soil roughness (σ). In the simulation, the antenna height was 4.75 m and soil composition was 78% sand, 10% silt, and 12% clay.

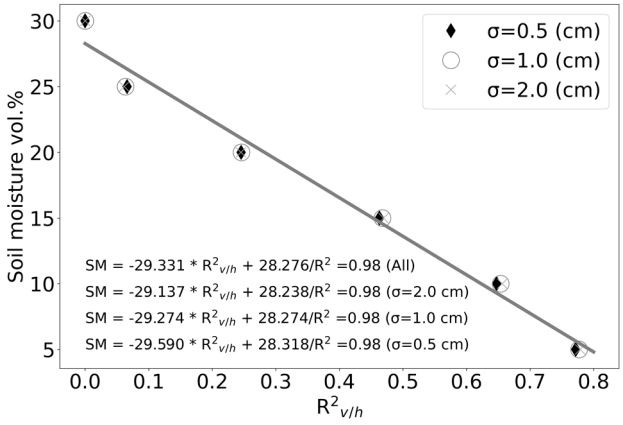

Fig. 4. Coefficient of determination between IP-H and IP-V ($\boldsymbol{R^2_{v/h}}$) versus SM for different levels of soil roughness ($\sigma = 0.5$, 1, and 2 cm).

before, during, and after irrigation were analyzed. Before irrigation, on May 12, 2022 (SM of approximately 7 vol.%), IP-H and IP-V waveforms oscillate in phase, yielding high $\boldsymbol{R^2_{v/h}} = 0.80$ [Fig. 5(a)]. During irrigation [Fig. 5(b)], on May 16, 2022 (SM of approximately 24 vol.%), the addition of water into the soil column modified the IP-V waveform mainly by reducing its amplitude for θ (between 9° and 14°). This was expected, as θ_B moves toward lower values of θ when SM increases [12] [Fig. 5(b)]. However, precise identification of θ_B was not straightforward because the amplitude and the frequency of the oscillations were not high enough for θ values between 9° and 14° [14] [Fig. 5(b)]. Most importantly, for $\theta > 14°$, IP-H and IP-V waveforms are almost totally in counter phase (the maxima position of IP-V matches the minima position of IP-H and vice versa), thus reducing $\boldsymbol{R^2_{v/h}}$ to 0.09 [Fig. 5(b)]. On May 19, 2022, two days after irrigation (SM of approximately 18 vol.%), IP-H and IP-V waveforms are partially in counter phase (for $\theta > 14°$), which slightly increased $\boldsymbol{R^2_{v/h}}$ to 0.19 compared to during irrigation ($\boldsymbol{R^2_{v/h}} = 0.09$) [Fig. 5(c)]. After irrigation, on June 12, 2022 (SM-10 of approximately 10 vol.%), $\boldsymbol{R^2_{v/h}}$, IP-H and IP-V waveforms were mainly in-phase with an increased $\boldsymbol{R^2_{v/h}}$ value of 0.75 [Fig. 5(d)]. Therefore, the relation obtained between $\boldsymbol{R^2_{v/h}}$ and SM when using simulations from the coherent specular reflection model remains consistent with actual observations from the SMIGOL-R instrument, demonstrating the feasibility of using $\boldsymbol{R^2_{v/h}}$ to track SM variations.

Analysis of a large number of IP waveforms acquired by different satellites when soil conditions were unchanged, revealed an effect of the satellite's azimuth angle on the IP-H and IP-V waveforms and thus on the calculated $\boldsymbol{R^2_{v/h}}$. For instance, Fig. 6 shows the IP recorded by GPS-8 and GPS-21 on May 10, 2022 with a time difference of approximately 2 h. The soil around the SMIGOL-R at this time was completely homogeneous, as no irrigation or other activity had occurred

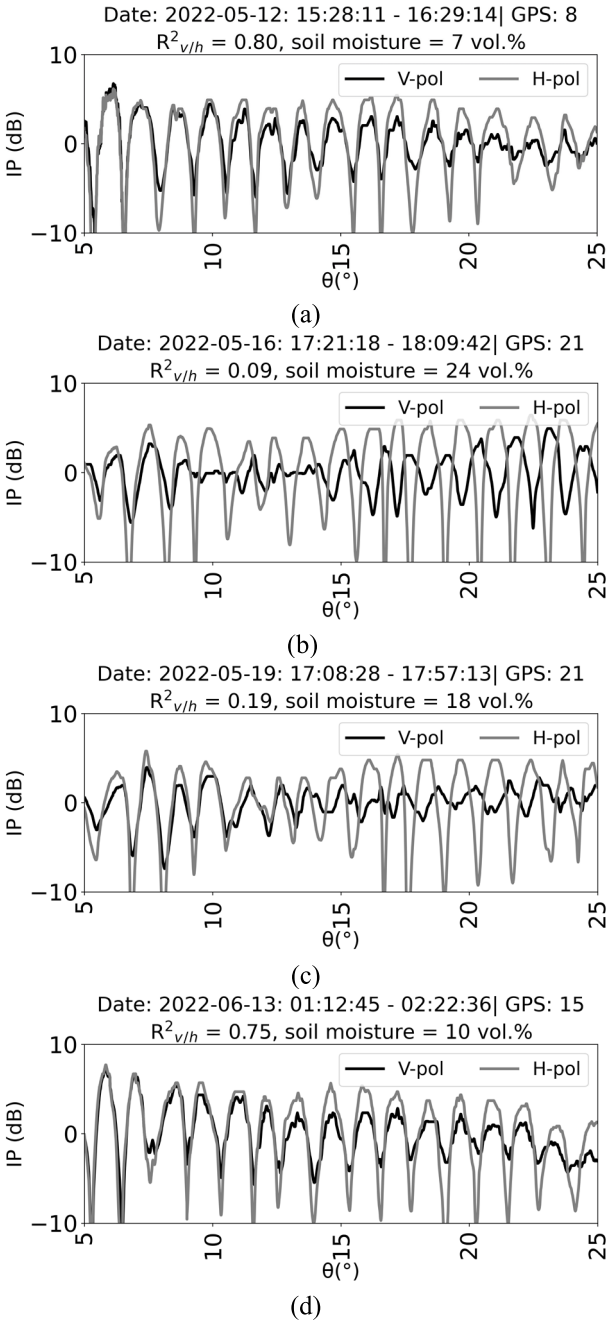

Fig. 5. IP profile for H-pol and V-pol acquired before (May 12, 2022 "a"), during (May 16, 2022 "b"), and after (May 19, 2022 "c" and June 13, 2022 "d") irrigation. Titles show acquisition date, time (start and end), and GPS number.

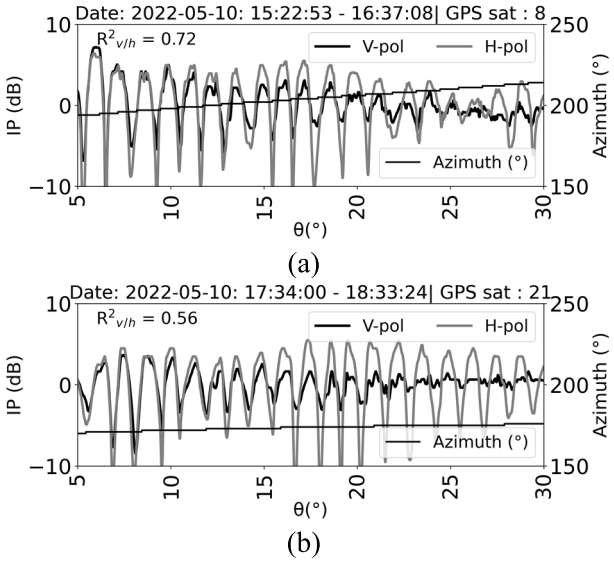

Fig. 6. IP profile for H-pol and V-pol acquired on May 10, 2022. (a) GPS-8. (b) GPS-21.

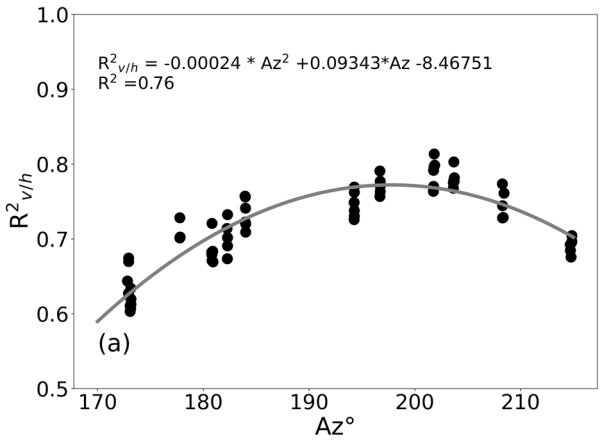

Fig. 7. Correlation between IP at V-pol and H-pol ($\boldsymbol{R^2_{v/h}}$) as a function of the satellite azimuth position (Az).

for a long time. Although having similar soil conditions at the two GPS acquisition times, $\boldsymbol{R^2_{v/h}}$ and, consequently, the estimated SM (Fig. 4) of GPS-8 ($\boldsymbol{R^2_{v/h}} = 0.72$ gives an estimated SM of 7.2 vol.%) and GPS-21 ($\boldsymbol{R^2_{v/h}} = 0.56$ gives an estimated SM of 11.9 vol.%) were different (difference in $\boldsymbol{R^2_{v/h}}$ and SM is 0.16 and 4.7 vol.%, respectively) (Fig. 6). A potential reason is the azimuth angle position of the GPSs during IP recording (the azimuth angle of GPS-8 and GPS-21 was ∼201° and ∼173°, respectively) [18]. To understand the effects of satellite azimuth angle on $\boldsymbol{R^2_{v/h}}$, it was calculated for each GPS acquisition between May 10 and 15, 2022 (i.e., stable dry soil conditions) and expressed as a function of the GPS azimuth angle (average of azimuth angle values during recording) (Fig. 7). Fig. 7 shows that for similar soil conditions, $\boldsymbol{R^2_{v/h}}$ varies between 0.6 and 0.8, and this variation depends on satellite azimuth angle ($R^2 = 0.76$), see Fig. 7. This relation illustrates the effect of azimuth angle position on the GPS signals recorded by SMIGOL-R.

C. SM Estimation From SMIGOL-R

In this section, the temporal variations of in situ SM and $\boldsymbol{R^2_{v/h}}$ between May 15, 2022 and December 31, 2022 were analyzed. Given the influence of azimuth angle position on $\boldsymbol{R^2_{v/h}}$ (Section IV), the obtained $\boldsymbol{R^2_{v/h}}$ was presented in groups with similar azimuth angles ($170° < \mathrm{Az}_{170-185} < 185°$, $185° < \mathrm{Az}_{185-200} < 200°$, $200° < \mathrm{Az}_{200-230} < 230°$), see Fig. 8. Fig. 8(a) shows that variations in satellite azimuth angle position cause a shift in $\boldsymbol{R^2_{v/h}}$ values, with this shift observed throughout the period of the experiment. Regardless of the group of azimuth angle, the $\boldsymbol{R^2_{v/h}}$ values inversely covary

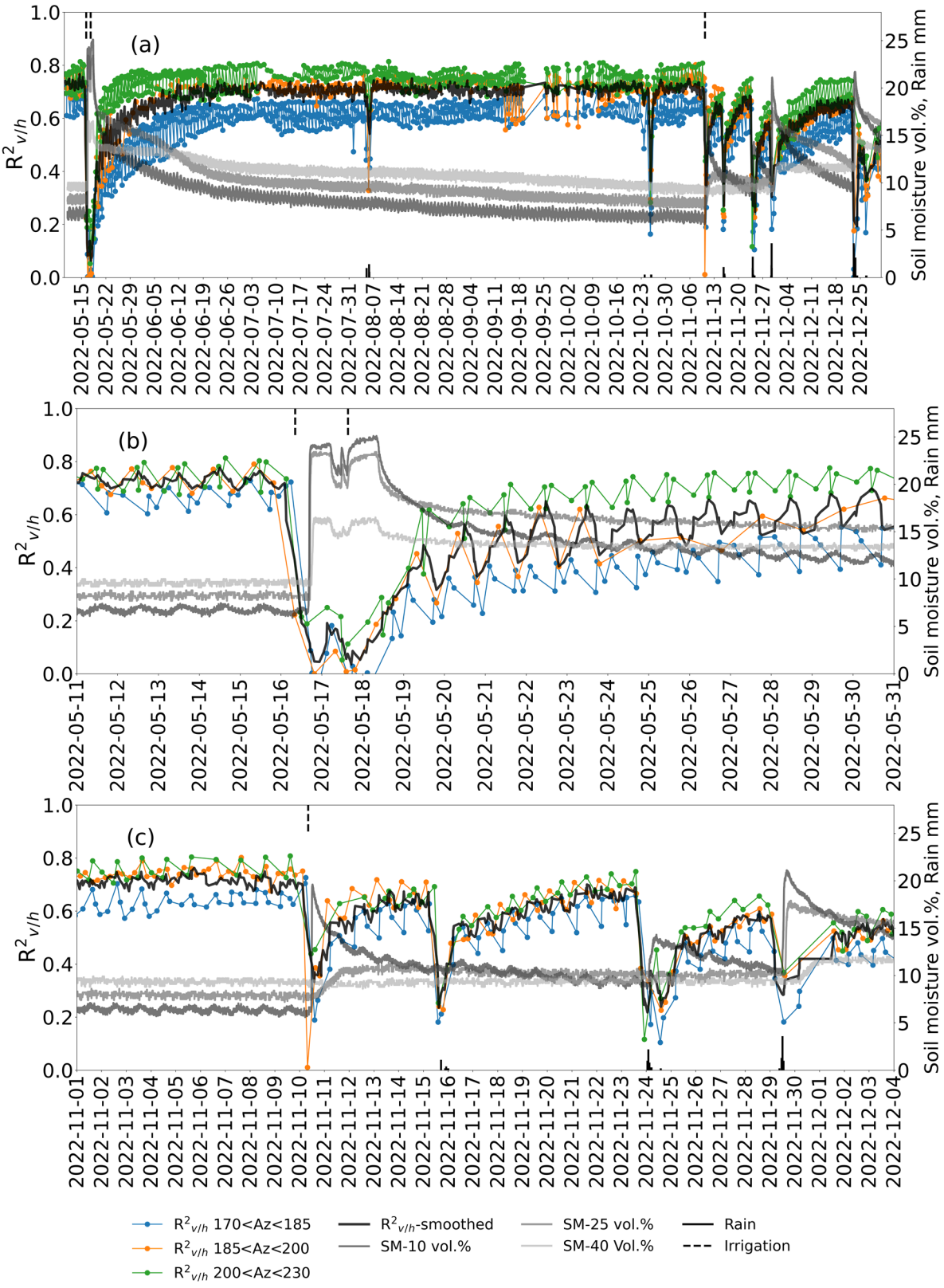

Fig. 8. (a) Temporal variation of the correlation between IP-V and IP-H ($\boldsymbol{R^2_{v/h}}$). (b) Selected 21-day period around the time of the first irrigation activity. (c) Selected 34-day period around the time of the second irrigation activity. Vertical lines show rain events. Dashed vertical lines show irrigation events.

with SM. $\boldsymbol{R^2_{v/h}}$ decreased from ∼0.7 on May 15, 2022 (SM-10 of approximately 7 vol.%) to ∼0.1 immediately after the first irrigation on May 16, 2022 [Fig. 8(a) and (b)]. During the first irrigation activities (between May 16 and 17), when SM-10 stabilized at around 25 vol.%, $\boldsymbol{R^2_{v/h}}$ remained low (∼0.1). On May 18, 2022 (just after irrigation), SM and $\boldsymbol{R^2_{v/h}}$ started decreasing and increasing, respectively. In contrast to the deeper root zone SMs (SM-25 and SM-40) between

May 18–20, SM-10 decreased quickly from ∼25 vol.% to ∼16 vol.%. $\boldsymbol{R^2_{v/h}}$ was also found to covary better with SM-10 variations than root zone SM, indicating that $\boldsymbol{R^2_{v/h}}$ is mostly sensitive to surface SM rather than the root zone SM [Fig. 8(a) and (b)] [11]. From June 20 to November 10 (before the second irrigation), $\boldsymbol{R^2_{v/h}}$ was stable (around 0.60, 0.70, and 0.78 for $Az_{170-185}$, $Az_{185-200}$, and $Az_{200-230}$, respectively) as SM-10 slightly decreased between 9.0 vol.% and 6 vol.%, indicating that $\boldsymbol{R^2_{v/h}}$ is not sensitive to slight variation in surface SM in dry conditions [19]. As for the first irrigation activity, $\boldsymbol{R^2_{v/h}}$ inversely covary with SM variations because of the irrigation applied on November 11. Similarly, the increase in moisture due to rain events observed between November 20 and December 25 caused a decrease in $\boldsymbol{R^2_{v/h}}$ values [Fig. 8(a) and (c)]. Fig. 8(b) and (c) shows that as irrigation starts, $\boldsymbol{R^2_{v/h}}$ decreases, while the SM sensors do not display an increase, as the IP waveform detects the presence of water on the top surface before water reaches the sensors installed at 10, 25, and 40 cm depths.

On August 5, a sudden decrease of $\boldsymbol{R^2_{v/h}}$ was observed simultaneously with a moderate rainfall of 4 mm (daily air temperature 44°) with no response from the SM-10 sensor. The same phenomena were observed on October 25 and November 15, where negligible rain events occurred (daily cumulative <2 mm) without any change in the SM-10 sensor. The decrease of $\boldsymbol{R^2_{v/h}}$ observed from these low precipitation events (daily cumulative <4 mm) was moderate (0.35), yet yielded a seemingly unrealistic increase in estimated SM of 10 vol.% when applying the equation in Fig. 4. Therefore, these instantaneous decreases and increases observed in $\boldsymbol{R^2_{v/h}}$ on August 5, October 25, and November 15 can likely be attributed to two factors. First, the presence of rain can affect both transmitted and multipath GNSS signals [20]. Second, there is a difference in sensing depth between the ThetaProbe SM-10 and GNSS signals (0–5 cm), with the assumption that SM at shallow depths (0–5 cm) may evaporate before reaching a depth of 10 cm due to the hot, dry conditions in Saudi Arabia.

The Savitzky–Golay temporal filter (a window length of 7) was applied to combine $\boldsymbol{R^2_{v/h}}$ of each azimuth angle group. The Savitzky–Golay filter can be applied because the temporal variations of $\boldsymbol{R^2_{v/h}}$ were similar regardless of the azimuth angle value, and the shift in $\boldsymbol{R^2_{v/h}}$ was almost constant and small (mostly <0.20). The results showed that the use of the Savitzky–Golay filter did not suppress the variations of $\boldsymbol{R^2_{v/h}}$ associated with the increase and decrease in SM (Fig. 8). The SM was estimated from $\boldsymbol{R^2_{v/h}}$ obtained with the Savitzky–Golay temporal filter using the equation in Fig. 4 and the results were compared to SM-10. The results showed that $\boldsymbol{R^2_{v/h}}$ provides a slightly biased estimate of SM-10 (−0.13 vol.%) with high accuracy (RMSE ∼1.5 vol.% and $R^2 = 0.80$) (Fig. 9). Fig. 9 shows a nonbiased estimation of SM-10 < 8 vol.%, a slight underestimation of −1.12 vol.% (RMSE = 1.76 vol.%) for SM-10 between 8 vol.% and 18 vol.%, and a slight overestimation of 1.27 vol.% for SM-10 vol.% > 18 vol.% (RMSE = 1.98 vol.%). The nonbiased estimation is attributed to the dry SM conditions when

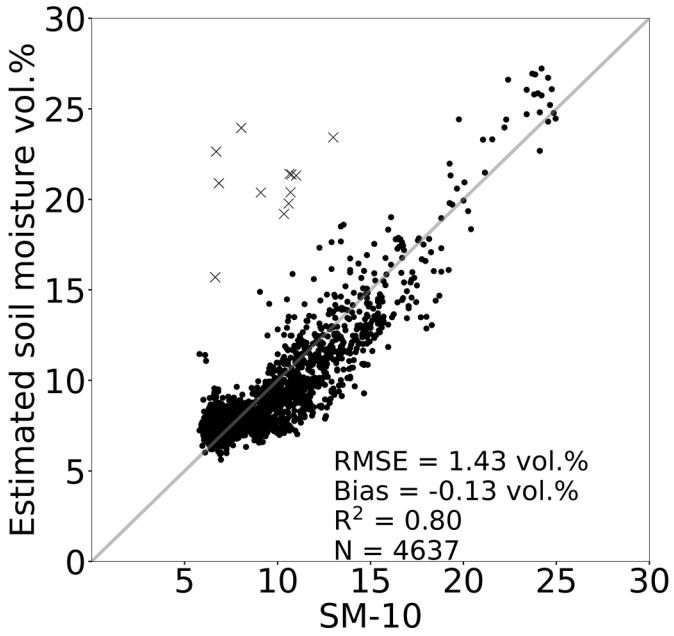

Fig. 9. Estimated SM versus in situ SM at 10 cm depth (SM-10). Samples represented with an "x" symbol belong to the period when irrigation commenced during which the IP signals detected the presence of water before it reached the sensor installed at a 10 cm depth and during light rain events (i.e., rainfall <4 mm) on August 5, October 25, and November 15.

the penetration depth of the L-band signal can reach 10 cm [11], [19]. The observed underestimation and overestimation were expected, given that the L-band GNSS-R signal is sensitive to the moisture in the top 5 cm [11] for wet soil conditions. Indeed, when SM-10 is between 10 vol.% and 18 vol.% (period of two days after the end of irrigation), SM-10 dries slower than SM in the top 5 cm, resulting in a lower SM estimate from the GNSS-R signals, which are more sensitive to moisture at 5 cm depth. Conversely, the observed overestimation, mainly for the highest SM values of ∼25 vol.% (during irrigation), can be attributed to the fact that the top 5 cm of soil received water before infiltration reached a 10 cm depth, resulting in an overestimation of moisture levels at SM-10 during irrigation.

V. Summary and Conclusion

The experiment was carried out over a bare and smooth surface to estimate the SM from the correlation between IP-V and IP-H waveforms. Theoretically, the IPT technique, which is based on the calculation of the Fresnel coefficient, assumes that the ground surface is smooth with respect to the GPS wavelength (i.e., it meets the Rayleigh criterion for the L-band). Winkel [21] reported a range of σ (2–5 cm) below which a surface is considered smooth for an L-band wave transmitted with θ between 5° and 30°. Future research will need to focus on testing the method developed herein under rough soil conditions. Since roughness affects H-pol and V-pol equally [14], it is anticipated that $\boldsymbol{R^2_{v/h}}$ can estimate the SM for rough soil up to a certain threshold of σ.

A stable $\boldsymbol{R^2_{v/h}}$ was observed during the dry period between the two irrigation activities, reflecting the robustness of the use of $\boldsymbol{R^2_{v/h}}$ to estimate SM. However, $\boldsymbol{R^2_{v/h}}$ was not sensitive

to the small decrease of moisture under dry conditions (in situ SM <7 vol.%), probably due to the high penetration depth of GNSS-transmitted signals into dry soil (penetration of L-band increases with decreasing SM) [19], [22]. Indeed, in a study conducted in areas of severe drought in Senegal (95% sand), Ha et al. [19] reported that when the transmitted signal penetrates deep into the soil, the reflected signal does not contain information on SM because the deep propagation of the transmitted wave within the soil affects its amplitude and phase (parameters used to estimate the SM).

The use of $\boldsymbol{R}^{2}_{v/h}$ to estimate SM shows satisfactory results for continuous monitoring at 10 cm depths. However, root zone SM is also a vital variable needed in hydrological applications. Leveraging previous studies exploring SM profile extrapolation, GNSS-R-derived SM could be used to estimate root zone moisture via an exponential filter [23] or by assimilating GNSS-R-derived surface SM into a hydrological model [24].

A method that leverages the high revisit time of GPS signals was developed to estimate SM over a bare and very smooth surface. The study progresses the work of [12] and [14] by providing a practical method to estimate SM at 10 cm depth with a high accuracy (RMSE ∼1.5 vol.%) using both IP-H and IP-V. Indeed, the developed method herein overcomes the uncertainty associated with the estimation of the notch position (θ_B), either from the calculation of the IP waveform envelope [12] or from the calculation of the phase difference between IP-V and IP-H waveforms [14]. Future work should focus on correcting azimuth effects and testing the method presented herein under rough soil conditions and in areas with vegetation cover. In addition, future work will consider the installation of SM sensors at a 2.5 cm depth to measure the SM in the 0–5-cm soil layer. Installing a network of SMIGOL-R receivers over a vast area will contribute to the calibration of satellite space missions dedicated to monitoring SM globally.

ACKNOWLEDGMENT

The authors would like to thank Fabio Viega de Camargo, Victor Angulo, and Jamal Elfarkh for helping in field experiments.

REFERENCES

[1] M. El Hajj, N. Baghdadi, M. Zribi, and H. Bazzi, "Synergic use of Sentinel-1 and Sentinel-2 images for operational soil moisture mapping at high spatial resolution over agricultural areas," *Remote Sens.*, vol. 9, no. 12, p. 1292, Dec. 2017, doi: 10.3390/rs9121292.

[2] J. Liang, G. Liang, Y. Zhao, and Y. Zhang, "A synergic method of Sentinel-1 and Sentinel-2 images for retrieving soil moisture content in agricultural regions," *Comput. Electron. Agricult.*, vol. 190, Nov. 2021, Art. no. 106485.

[3] S. Paloscia, S. Pettinato, E. Santi, C. Notarnicola, L. Pasolli, and A. Reppucci, "Soil moisture mapping using Sentinel-1 images: Algorithm and preliminary validation," *Remote Sens. Environ.*, vol. 134, pp. 234–248, Jul. 2013.

[4] M. El Hajj, N. Baghdadi, H. Bazzi, and M. Zribi, "Penetration analysis of SAR signals in the C and L bands for wheat, maize, and grasslands," *Remote Sens.*, vol. 11, no. 1, p. 31, Dec. 2018.

[5] M. El Hajj et al., "Evaluation of SMOS, SMAP, ASCAT and Sentinel-1 soil moisture products at sites in southwestern France," *Remote Sens.*, vol. 10, no. 4, p. 569, Apr. 2018.

[6] R. Oliva et al., "SMOS radio frequency interference scenario: Status and actions taken to improve the RFI environment in the 1400–1427-MHz passive band," *IEEE Trans. Geosci. Remote Sens.*, vol. 50, no. 5, pp. 1427–1439, May 2012.

[7] J.-P. Wigneron et al., "SMOS-IC data record of soil moisture and L-VOD: Historical development, applications and perspectives," *Remote Sens. Environ.*, vol. 254, Mar. 2021, Art. no. 112238.

[8] M. F. McCabe et al., "The future of Earth observation in hydrology," *Hydrol. Earth Syst. Sci.*, vol. 21, no. 7, pp. 3879–3914, Jul. 2017.

[9] K. M. Larson, E. E. Small, E. Gutmann, A. Bilich, P. Axelrad, and J. Braun, "Using GPS multipath to measure soil moisture fluctuations: Initial results," *GPS Solutions*, vol. 12, no. 3, pp. 173–177, Jul. 2008.

[10] C. C. Chew, E. E. Small, K. M. Larson, and V. U. Zavorotny, "Effects of near-surface soil moisture on GPS SNR data: Development of a retrieval algorithm for soil moisture," *IEEE Trans. Geosci. Remote Sens.*, vol. 52, no. 1, pp. 537–543, Jan. 2014.

[11] V. U. Zavorotny, K. M. Larson, J. J. Braun, E. E. Small, E. D. Gutmann, and A. L. Bilich, "A physical model for GPS multipath caused by land reflections: Toward bare soil moisture retrievals," *IEEE J. Sel. Topics Appl. Earth Observ. Remote Sens.*, vol. 3, no. 1, pp. 100–110, Mar. 2010.

[12] N. Rodriguez-Alvarez et al., "Soil moisture retrieval using GNSS-R techniques: Experimental results over a bare soil field," *IEEE Trans. Geosci. Remote Sens.*, vol. 47, no. 11, pp. 3616–3624, Nov. 2009.

[13] A. Egido et al., "Global navigation satellite systems reflectometry as a remote sensing tool for agriculture," *Remote Sens.*, vol. 4, no. 8, pp. 2356–2372, Aug. 2012.

[14] A. Alonso-Arroyo et al., "Improving the accuracy of soil moisture retrievals using the phase difference of the dual-polarization GNSS-R interference patterns," *IEEE Geosci. Remote Sens. Lett.*, vol. 11, no. 12, pp. 2090–2094, Dec. 2014.

[15] G. Lérondel and R. Romestain, "Fresnel coefficients of a rough interface," *Appl. Phys. Lett.*, vol. 74, no. 19, pp. 2740–2742, May 1999.

[16] P. Beckmann and A. Spizzichino, *The Scattering of Electromagnetic Waves From Rough Surfaces*, vol. 1. Norwood, MA, USA: Artech House, 1987, p. 511.

[17] M. Hallikainen, F. Ulaby, M. Dobson, M. El-Rayes, and L.-K. Wu, "Microwave dielectric behavior of wet soil—Part 1: Empirical models and experimental observations," *IEEE Trans. Geosci. Remote Sens.*, vol. GE-23, no. 1, pp. 25–34, Jan. 1985.

[18] X. Chang, T. Jin, K. Yu, Y. Li, J. Li, and Q. Zhang, "Soil moisture estimation by GNSS multipath signal," *Remote Sens.*, vol. 11, no. 21, p. 2559, Oct. 2019.

[19] M.-C. Ha et al., "GNSS-R monitoring of soil moisture dynamics in areas of severe drought: Example of Dahra in the Sahelian climatic zone (Senegal)," *Eur. J. Remote Sens.*, vol. 55, pp. 1–19, Dec. 2022.

[20] R. Balasubramaniam and C. Ruf, "Characterization of rain impact on L-band GNSS-R ocean surface measurements," *Remote Sens. Environ.*, vol. 239, Mar. 2020, Art. no. 111607.

[21] J. O. Winkel, "Modeling and simulating GNSS signal structures and receivers," Ph.D. dissertation, Dept. Civil Eng. Environ. Sci., Univ. Bundeswehr Munich, Munich, Germany, 2000.

[22] V. Zavorotny et al., "Seasonal polarimetric measurements of soil moisture using tower-based GPS bistatic radar," in *Proc. IEEE Int. Geosci. Remote Sens. Symp.*, Jul. 2003, pp. 781–783.

[23] Y. Yang et al., "An exponential filter model-based root-zone soil moisture estimation methodology from multiple datasets," *Remote Sens.*, vol. 14, no. 8, p. 1785, Apr. 2022.

[24] P. Heidary, L. Farhadi, and M. U. Altaf, "Estimation of root zone soil moisture profile by reduced-order variational data assimilation using near surface soil moisture observations," *IEEE J. Sel. Topics Appl. Earth Observ. Remote Sens.*, vol. 15, pp. 2394–2409, 2022.

Marcel M. El Hajj received the Ph.D. degree in geomatics and remote sensing from AgroParisTech University, Paris, France, in 2015.

He was a Research Engineer with the National Research Institute of Science and Technology for Environment and Agriculture, France. He worked as a Modeling Researcher at Intelligence Technology Knowledge, Montpellier, France. He has been a Post-Doctoral Researcher with the King Abdullah University of Sciences and Technology, Thuwal, Saudi Arabia, since 2021. His main field of interest is the use of microwave, optical, and LiDAR remote sensing data for land surface applications.

Susan C. Steele-Dunne (Member, IEEE) received the S.M. and Ph.D. degrees in hydrology from the Massachusetts Institute of Technology, Cambridge, MA, USA, in 2002 and 2006, respectively.

She has been with the Faculty of Civil Engineering and Geosciences, Delft University of Technology, Delft, The Netherlands, since 2008, where she is currently a Professor with the Department of Geoscience and Remote Sensing. She leads the M-WAVE Group, which performs research from field to global scales, combining in situ and spaceborne data to improve the understanding of microwave interactions with vegetation. Her research interests include data assimilation, modeling, and machine learning to exploit spaceborne radar instruments for applications in ecosystem and agricultural monitoring.

Samer K. Almashharawi received the M.Sc. degree in environmental science and engineering from the King Abdullah University of Science and Technology, Thuwal, Saudi Arabia, in 2011, where he has been a Research Specialist since 2012. His main fields of interest include the use of cosmic ray neutron sensors and in situ data for precision agriculture applications.

Xuemeng Tian received the Ir. degree from the Delft University of Technology, Delft, The Netherlands, in 2022. She is currently pursuing the Ph.D. degree with the Laboratory of Geo-Information Science and Remote Sensing, Wageningen University and Research and OpenGeoHub Foundation, Wageningen, The Netherlands.

Her research interests include digital soil mapping, soil organic carbon, and remote sensing.

Kasper Johansen received the Ph.D. degree in remote sensing from the University of Queensland, Brisbane, Australia, in 2007.

Since 2017, he has been a Research Scientist with the King Abdullah University of Science and Technology, Thuwal, Saudi Arabia. He is also an Associate Editor of the Frontiers in Remote Sensing. His main research interests are focused on processing and analyzing high spatial resolution remotely sensed multispectral, hyperspectral, LiDAR, and thermal image data acquired from satellite, airborne, and UAV-based sensors to extract ecologically meaningful information.

Omar A. López Camargo (Student Member, IEEE) received the B.S. degree in electronic engineering from the National University of Colombia, Bogota, Colombia, in 2020, and the M.S. degree in environmental science and engineering from the King Abdullah University of Science and Technology (KAUST), Thuwal, Saudi Arabia, in 2022, where he is currently pursuing the Ph.D. degree in environmental science and engineering, with a primary focus on remote sensing. His expertise lies in the utilization of agile robots, unmanned aerial vehicles (UAVs), and satellites for vegetation assessment, particularly in areas such as biodiversity mapping and climate change monitoring and mitigation.

Adria Amezaga-Sarries received the Ph.D. degree in ground-based synthetic aperture radar from Universitat Politècnica de Catalunya, Barcelona, Spain, in 2020, where he was involved in GNSS Reflectometry and New Space research projects. He is the Co-Founder of Microwave Sensors and Electronics SL (MWSE), where he leads mixed-signal, RF, and microwave design tasks for remote sensing applications, including spaceborne GNSS receivers, microwave radiometers, and ground-based radar systems. His main research interests include the application of multifrequency in ground-based synthetic aperture radar systems.

Andreu Mas-Viñolas received the bachelor's degree in aerospace engineering and telecommunications engineering from the Politechnic University of Catalunya, Barcelona, Spain, in 2022, where he is currently pursuing the M.Sc. degree in telecommunications, specializing in remote sensing.

Since 2022, he has been working on the development of near-ground remote sensing systems with Microwave Sensors and Electronics Company. His main fields of interest include the development of remote sensing technologies to study the evolution of natural phenomena such as climate change.

Matthew F. McCabe received the Ph.D. degree in civil and environmental engineering from the University of Newcastle, Callaghan, Australia, in 2003.

He is currently a Professor of remote sensing and water security and the Director of the KAUST Climate and Livability Initiative, King Abdullah University of Science and Technology, Thuwal, Saudi Arabia. His research explores a range of multidisciplinary issues around water and food security, climate change impacts, precision agriculture, and water resources monitoring and modeling.